water

MDPI

Article

Mapping Dynamic Water Fraction under the Tropical Rain Forests of the Amazonian Basin from SMOS Brightness Temperatures

Marie Parrens [1,*], Ahmad Al Bitar [1], Frédéric Frappart [2,3], Fabrice Papa [2,4], Stephane Calmant [2], Jean-François Crétaux [2], Jean-Pierre Wigneron [5] and Yann Kerr [1]

1 Centre d'Etudes Spatiales de la BIOsphère (CESBIO—Université de Toulouse, CNES, CNRS, IRD), UMR5126, BPI 2801, 31401 Toulouse CEDEX 9, France; ahmad.albitar@cesbio.cnes.fr (A.A.B.); yann.kerr@cesbio.cnes.fr (Y.K.)

2 Laboratoire d'Etudes en Géophysique et Océanographie Spatiales (LEGOS), UMR5566, Université de Toulouse, CNES, CNRS, IRD, Observatoire Midi-Pyrénées (OMP), 14 Avenue Edouard Belin, 31400 Toulouse, France; frederic.frappart@legos.obs-mip.fr (F.F.); fabrice.papa@ird.fr (F.P.); stephane.calmant@ird.fr (S.C.); jean-francois.cretaux@legos.obs-mip.fr (J.-F.C.)

3 Géosciences Environnement Toulouse (GET), UMR5563, Université de Toulouse, CNES, CNRS, IRD, Observatoire Midi-Pyrénées (OMP),14 Avenue Edouard Belin, 31400 Toulouse, France

4 Indo-French Cell for Water Sciences (IFCWS), IRD-IISc-NIO-IITM Joint International Laboratory, Bangalore 560012, India

5 INRA, UMR 1391 ISPA, F-33140 Villenave d'Ornon, Bordeaux, France; wigneron@bordeaux.inra.fr

* Correspondence: marie.parrens@cesbio.cnes.fr; Tel.: +33-5-6155-8531

Academic Editor: Y. Jun Xu
Received: 23 February 2017; Accepted: 11 May 2017; Published: 17 May 2017

Abstract: Inland surface waters in tropical environments play a major role in the water and carbon cycle. Remote sensing techniques based on passive, active microwave or optical wavelengths are commonly used to provide quantitative estimates of surface water extent from regional to global scales. However, some of these estimates are unable to detect water under dense vegetation and/or in the presence of cloud coverage. To overcome these limitations, the brightness temperature data at L-band frequency from the Soil Moisture and Ocean Salinity (SMOS) mission are used here to estimate flood extent in a contextual radiative transfer model over the Amazon Basin. At this frequency, the signal is highly sensitive to the standing water above the ground, and the signal provides information from deeper vegetation density than higher-frequencies. Three-day and (25 km × 25 km) resolution maps of water fraction extent are produced from 2010 to 2015. The dynamic water surface extent estimates are compared to altimeter data (Jason-2), land cover classification maps (IGBP, GlobeCover and ESA CCI) and the dynamic water surface product (GIEMS). The relationships between the water surfaces, precipitation and in situ discharge data are examined. The results show a high correlation between water fraction estimated by SMOS and water levels from Jason-2 ($R > 0.98$). Good spatial agreements for the land cover classifications and the water cycle are obtained.

Keywords: water fraction extent; L-band; Amazon Basin

1. Introduction

Terrestrial surface water covers only about 5% of the Earth's ice-free land surface [1,2], but plays a key role in global biogeochemistry, hydrology and wildlife diversity [3,4]. Consequently, it is critical to monitor the distribution of terrestrial water at large spatial and high temporal scales [5–8]. The work in [9] estimates that nearly two-thirds of all terrestrial freshwater wetlands disappeared between 1997 and 2011. A more recent study used three million Landsat images to provide a high resolution map of

surface water extent [10]. The authors of this study estimated that 90,000 km^2 of permanent surface water had disappeared between 1984 and 2015.

Several different methods based on mapping water bodies from remote sensing datasets were used since the development of the Earth's space observations: (1) visible; (2) infrared; (3) active microwave; (2) passive microwave and; (4) hybrid approach (passive and active microwave). Each method offers varying degrees of success in providing quantitative estimates of wetlands and inundation extents.

Water surface can be sensed by optical remote sensing methods. These methods typically exploit the absorption of longer wavelengths of light in water, especially the near and shortwave infrared parts of the electromagnetic spectrum [11,12]. Optical remote sensing provides very accurate mapping of water bodies. For example, [13] senses lakes with a spatial resolution of 15 m, whereas [14] sensed global water bodies at 30-m resolution using the Landsat data. The majority of the studies using optical remote sensing for water bodies' detection provided only one snapshot of the hydrology stage. Due to the low revisit time of the optical sensors, few maps of a large area are available, and the minimum and/or the maximum of the flooded area are not always observed. The detection of sudden changes impacting the hydrologic cycle [10] is also not sensed with accuracy. These limitations are crucial issues for hydrology application. However, some studies [15,16] managed to follow the temporal dynamics of the water surface in specific places. The most important limitation of the optical sensors is their inability to penetrate clouds and dense vegetation cover, which is essential during tropical wet seasons over the Amazon Basin.

Active microwave (scatterometers and Synthetic Aperture Radar (SAR)) is also sensitive to the water surface and has the ability to penetrate clouds and, to a certain extent, vegetation. Open water surfaces are generally characterized by low backscattering coefficients. Contrary to passive microwave, the signal is more contaminated by the vegetation. The spatial resolution of scatterometers is about 25–50 km, whereas the SAR provides higher resolution, typically around 10–150 m. Several studies have shown the ability of active microwave to map surface water at regional scales, such as over the Amazon region [17] and over the Arctic region [18]. Satellite altimeters are radars that observe at nadir to measure surface topography. They provide accurate measurements of water heights in rivers, lakes and wetlands [19–21]. Due to their high spatial resolution, altimeters do not provide sufficient spatial coverage to analyze the water bodies' temporal dynamics, except in polar regions [22]. The future Surface Water Ocean Topography (SWOT) mission [23] intended to be launched in 2021 is expected to provide K-band SAR interferometry, enabling continental altimetry.

Passive microwaves are sensitive to the distribution of liquid water in the landscape; they can operate day and night for all weather conditions. However, they are limited by a low spatial resolution (approximately 30 km). They can sense only large wetlands or regions where the cumulative area of small wetlands comprises a significant portion of the field of view. Consequently, they provide the capability to map the temporal evolution of surface water over the land surface due to their high temporal resolution. In previous studies, passive microwave measurements have shown the capability to sense the dynamics of terrestrial surface water at coarse resolution [24–31]. The basic principle of the surface water measurements based on passive microwave is explained by the difference of the emissivity between the water and the soil. Flooding surfaces decrease the emissivity in both vertical (V) and horizontal (H) polarization and increase the difference between the two polarizations, especially at low frequencies. This approach produces ambiguous estimation of surface water over regions with mixtures of open water and other complex surfaces (topography effects). The work in [26,27] has extensively studied the inundation area over the Amazon Basin with the Scanning Multichannel Microwave Radiometer (SMMR). However, their studies focus essentially on a restricted area close to Manaus town from 1979 to 1987.

Hybrid approaches combine the strengths of different types of sensors. For example, altimetry data are characterized by a high spatial resolution and a low temporal resolution and can be combined with passive microwave data having low spatial resolution and a high temporal resolution to obtain a product with both high temporal and spatial resolution. The Global Inundation Extent

from Multiple-Satellites (GIEMS) products are based on merged data from passive (Special Sensor Microwave/Imager (SMM/I)), active microwave (European Remote Sensing satellite (ERS)) and data from an optical sensor (Advanced Very High Resolution Radiometer (AVHRR)) [32].

Table 1 presents the major studies related to the observation and detection of water bodies from space by using the techniques presented above. Visible and infrared remote sensing methods were extensively used, but provided static maps of water bodies at the global scale or a dynamic map at the regional scale [15,33]. A lack of studies concerning dynamic water surface extent from 2013 to the present is clearly identified in this table.

The floodplains and wetlands of the Amazon River are important in terms of water volume and in terms of fluxes between the land and the atmosphere. Mapping water fraction under the Amazon tropical dense forest is challenging, but sensing water under dense vegetation remains a key issue in the remote sensing scientific community.

In this study, we developed a method to map the temporal evolution of the water bodies at coarse spatial resolution and weekly temporal resolution by using a microwave sensor at L-band (1.4 GHz) called Soil Moisture Ocean Salinity (SMOS) over the Amazon Basin. The SMOS satellite operates at L-band, and it was shown that this frequency is the most suitable, being less impacted by vegetation than higher frequencies [34–36]. Originally, the SMOS satellite was dedicated to sense soil moisture over land surfaces and the ocean salinity. The SMOS physical signal (brightness temperature) is highly impacted by the presence of standing water over the ground.

Our motivation is to use a contextual radiative transfer model and a single dataset to estimate the water fraction over the tropical basin. The area of study and the datasets used in this work are presented in the Section 2 and 3, respectively. Section 4 presents the algorithm permitting retrieving the water fraction extent from the SMOS data, and Section 5 contains the results and the validation. The discussion and conclusions are presented in Sections 6 and 7.

Table 1. List of selected scientific papers on the observation of the water surface over the continents from space. References, area of study and sensors are shown.

Remote Sensing Approach	Reference	Area of Study	Sensors	Frequency
Passive microwave	[27]	Amazon Basin	SSMR	Q-band
	[29]	Boreal regions	SSM/I-SSMR	K- and Ka-band
	[37]	North Eurasian	AMSR-E-QSCAT	C-band
Active microwave		See [38] for a review of the SAR technique		
	[17]	Amazon Basin	ENVISAT SAR	L-band
	[39]	High latitude regions	ENVISAT ASAR	C-band
	[40]	Mekong basin	ENVISAT ASAR	C-band
	[41]	Global scale	ENVISAT ASAR	C-band
	[22]	Boreal regions	Topex-Poseidon	C-band
Hybrid approaches	[42]	Global scale	SSM/I, ERS, AVHRR	Ka- and C-band
	[32]	Global scale	SSM/I, ERS, AVHRR	Ka- and C-band
	[43]	Global scale	SSM/I, ERS, AVHRR	Ka- and C-band
	[37]	Global scale	SSM/I, SSMI/S, ERS, QSAT, ASCAT	Ku- and C-band
Optical and infrared	[44]	Okavango Delta	AVHRR	-
	[45]	Brahmaputra	AVHRR	-
	[46]	Inner Niger Delta	MODIS	-
	[47]	China	MODIS	-
	[33]	Mekong Delta	MODIS	-
	[10]	Global scale	Landsat	-

2. Study Areas

This study focuses on the Amazon Basin, which is the largest tropical basin with an area of approximately 6,000,000 km^2 and contributes up to 15% of the global river discharge to the ocean (approximately 200,000 m^3s^{-1} discharge). With a sediment load of three million tons near its mouth [48] and drainage area covers about 6,200,000 km^2, almost 5% of all of the continental masses, the

Amazon Basin is one of the most impressive hydrological basins of the world. The Amazon is highly interconnected by floodplain channels, resulting in complex flow patterns. Figure 1 presents the Amazon Basin with the main rivers and floodplains. Covering more than 300,000 km^2, the Amazon extensive floodplains play a crucial role for global climate and biodiversity, but they are still poorly monitored at a large scale, limiting our understanding of their role in flood hazard, carbon production, sediment transport, nutriment exchange and air-land interactions. Surface water stored in floodplains represents about half of the terrestrial water storage and 15–20% of the water that flowed out of the Amazon floodplains [49–53]. Because it extends over two hemispheres, the Amazon region is characterized by several rainfall regimes. Rainfall shows opposing phases between the Northern and the Southern Hemisphere with a rainy season in austral winter in the Northern Hemisphere and summer in the Southern Hemisphere. The rainfall shows a gradient from northwest to southeast with decreasing rainfall amount and increasing length in the dry season. For the eastern part of the basin, the rainy season occurs from March–May, and the dry season prevails from September–November. For the northern regions, low rainfall seasonality is observed with wet conditions throughout the year. For more information on the Amazon hydrological regime, see [54–56].

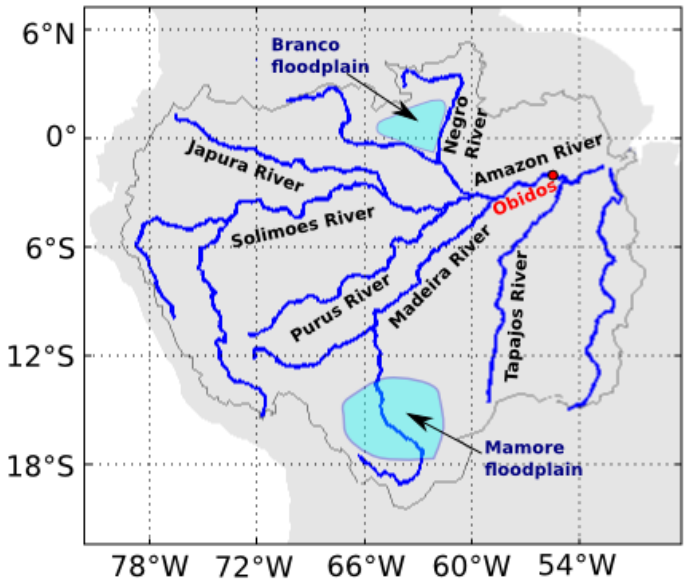

Figure 1. Map of the Amazon Basin with the main rivers and floodplains.

3. Data

This section describes the data used to compute the water fraction extent from passive microwave at L-band (SMOS data, topography data and skin temperature) and the data used to compare and validate this product (precipitation data, static land cover maps, other dynamic water fraction products, water level from altimetry and in situ river discharge data).

3.1. L-Band Brightness Temperatures from SMOS

The SMOS mission is a joint program of the European Space Agency (ESA), the Centre National d'Etudes Spatiales (CNES) and the Centro para el Desarrollo Teccnologico Industrial (CDTI) in the framework of the Earth Explorer Opportunity Mission initiative. It is the first satellite specifically dedicated to soil moisture retrievals with a passive microwave radiometer at 1.4 GHz (L-band). The physical signal of SMOS is the Brightness Temperature (TB). This signal is highly sensitive to the water under the ground [34]. Clouds and rain have a negligible effect [57], and the atmospheric contribution is limited and known [34]. The microwave signal is to a lesser extent sensitive to the vegetation, but actually, the L-band signal is less impacted by the vegetation than higher frequencies.

SMOS has a Sun-synchronous orbit at a 757-km altitude with a 06:00 LST ascending Equator crossing time and an 18:00 LST descending Equator crossing time. The globe is fully imaged twice every three days. The main innovative feature of SMOS is the capability for multi-incidence-angle observations at full polarization across a 900-km swath. In this study, the SMOS Level (L) 3 TB (RE04v300) products [58] produced by the Centre Aval de Traitement des Données SMOS (CATDS) are used. These data are projected on the Equal-Area Scalable Earth (EASE) Grid 2 [59] with a spatial resolution of 25 km × 25 km. The main differences between the SMOS L3 TB and the other lower levels of data are: (i) the L3 TB products are expressed at the top of the atmosphere over the terrestrial reference frame (H and V); and (ii) they are bin averaged every 5° from 2.5°–62.5°. In the present study, SMOS L3 TB were used from 2010–2015 over the Amazon Basin. Angles of 32 ± 5°, 37 ± 5°, 42 ± 5° and 47 ± 5° in both H and V polarization were considered to retrieve the water fraction over the tropical basin. The SMOS data were downloaded from the CATDS servers (www.catds.fr).

3.2. Topography

The digital elevation model obtained by the Shuttle Radar Topography Mission (SRTM) [60] with a spatial resolution of 30 arc sec(approximately 1 km) was used over the Amazon Basin. These data result from the Global 30 Arc-Second Elevation (GTOPO30) computed at the U.S. Geological Survey's EROS Data Center (USGS) and were available at https://Ita.cr.usgs.gov/GOTO30. The elevation and topographic index maps over the Amazon watersheds were computed by averaging all of the SRTM elevation values present in an SMOS pixel (Figure 2). These data are used to flag areas with an elevation higher than 500 and/or a topographic index indicated as moderate in the SMOS flag.

3.3. Skin Temperature

The surface skin temperature produced by the European Centre for Medium-range Weather Forecasting (ECMWF) was used in this study. This product was obtained by the SMOS L3 preprocessor, which computed the spatiotemporal average of the ECMWF reanalysis products on the EASE 2.0 grid.

3.4. Precipitation Data

Precipitation measured by the Tropical Rainfall Measuring Mission (TRMM) were used over the entire Amazon Basin from 2010–2015. TRMM is a joint mission between NASA and the Japan Aerospace Exploration (JAXA) Agency and provides rainfall estimates at 0.25° × 0.25° spatial resolution. The TRMM-3B42 product [61] uses microwave data to calibrate the infrared-derived estimates and creates estimates that contain microwave-derived rainfall estimates when and where microwave data are available and the calibrated infrared estimates where microwave data are not available.

3.5. Static Land Cover Maps

The International Geosphere-Biosphere Programme (IGBP), the GlobeCover land cover classification and the ESA CCI maps were used. The IGBP land cover map was obtained using images from the Moderate Resolution Imaging Spectroradiometer (MODIS) with a spatial resolution of 0.005° during 2001–2012 [62]. The GlobeCover land surface map is based on data from the Advanced Very High Resolution Radiometer (AVHRR) data and is at a 1-km spatial resolution. Data were acquired during 1992–1993 [63]. Recently, a new release of the ESA Climate Change Initiative (CCI) Land Cover map was made available [64]. The new water/no water global mask at 150 m was built on previous achievements using SAR systems and further improved thanks to a combination with recent Landsat-derived products. This dataset was based on acquisitions from the years 200–2012. Data can be downloaded at: http://www.esa-landcover-cci.org/?q=node/162. For the three products, the water classes were aggregated and re-sampled on the EASE v2.0 grid to obtain the water fraction (%) present in each cell of the EASE v2.0 grid. The three products are static and are presented in Figure 2.

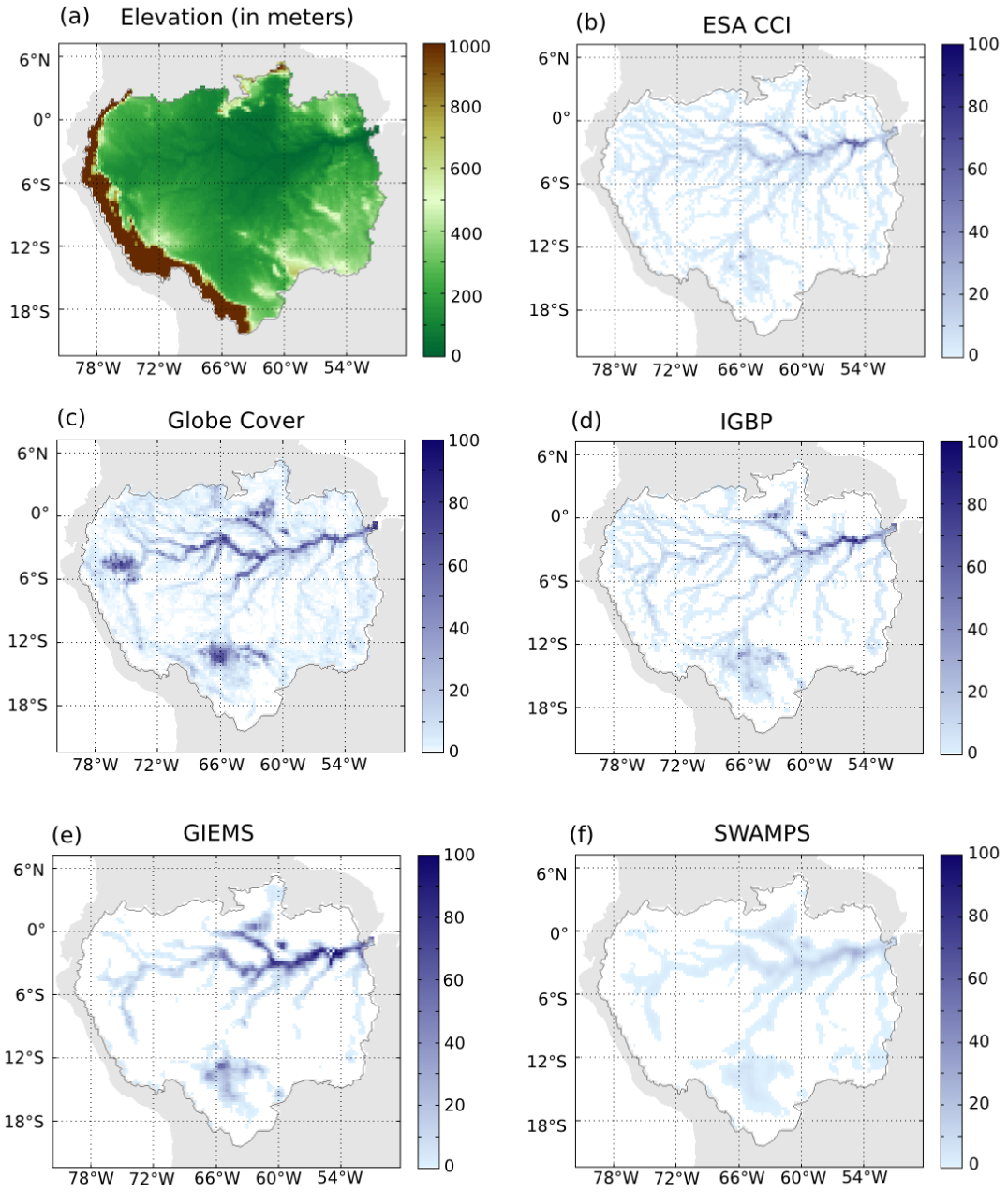

Figure 2. (**a**) Elevation (in meters) of the Amazon Basin from the SRTM data rescaled in the EASE v2.0 grid; spatial distribution of the water surface from: (**b**) ESA CCI; (**c**) IGBP; (**d**) Globe Cover; (**e**) average inundation extent from GIEMS from 1993–2007 over the Amazon Basin; and (**f**) average inundation extent from Surface Water Microwave Product Series (SWAMPS) from 2010–20over the Amazon Basin.

3.6. Dynamics and Climatoloy of Water Fraction Data

The GIEMS products provided a long-term global map of inundation at coarse resolution by merging passive and active data (SSM/I, ERS, AVHRR) from 1993–2007 at monthly time steps. The GIEMS product is gridded on an equal area grid of 0.25° × 0.25° at the Equator. Over highly vegetated areas, the GIEMS product has some limitations. For example, over the Amazon Basin, the GIEMS product has a tendency to overestimate higher inundation fractions [32]. This product is fully described in [42]. These data were subsequently employed in estimating surface water storage variations in large river basins [50,65,66]. To be compared with our data, the GIEMS product was

averaged during the full period and considered as a static climatological product. Figure 2 shows the temporal GIEMS average over the Amazon Basin from 1993–2007.

The recent Surface Water Microwave Product Series (SWAMPS) data provided daily surface water globally at 25-km resolution from 1992–2013. This product was based on the combination of passive and active microwave sensors (SSM/I, SSMIS, ERS, QuikSCAT, ASCAT) and visible sensors (MODIS). The data are described in detail and validated in [37]. In our study, only data from 2010–2013, coinciding with SMOS data availability, over the Amazon Basin were considered. Figure 2 shows the temporal SWAMPS average over the Amazon Basin from 2010–2013.

3.7. Water Level from Satellite Altimetry

In the Amazon Basin, water level (in meters) time series for virtual stations calculated from the Jason-2 altimeter satellite over the period 2008–2012 were downloaded from the Hydroweb database (http://hydroweb.theia-land.fr/). The Jason-2 satellite was launched on 20 June 2008 in the follow-on mission to the Jason-1 satellite (2002–2008, CNES/NASA). It operates at Ku-band (13.575 GHz) and C-band (5.3 GHz) and has a time period of ∼9.9 days [67]. The water level computation method and the location of the virtual stations are presented in [68]. In the present study, water level time series over 83 virtual stations from 2010–2012 inclusive were used.

3.8. In Situ River Discharge Data

Monthly in situ discharge (m^3/s) observations for the Amazon River were obtained from the Obidos gauge station (1°00′ S, 55°00′ W) for the period of January 2010–March 2014. Data are available on Hidroweb (http://www.hidroweb.ana.gov.fr) from the Brazilian water agency.

4. Methods

This section describes the approach used to derive surface water extent (expressed in %) contained in an SMOS pixel from the SMOS L3 TB. The contextual radiative transfer model and the selection of two reference points are described below, followed by the statistical method used to compare and validate the SWAF product.

4.1. Contextual Radiative Transfer Model to Retrieve the Water Fraction under Dense Forests

4.1.1. Description of the SWAF Algorithm

It is well known that the microwave emission is highly impacted by the dielectric constant [57]. In the present algorithm, we assumed that over the tropical basins, the pixels are only composed of two contributions: the water and the forest, such as represented in Figure 3.

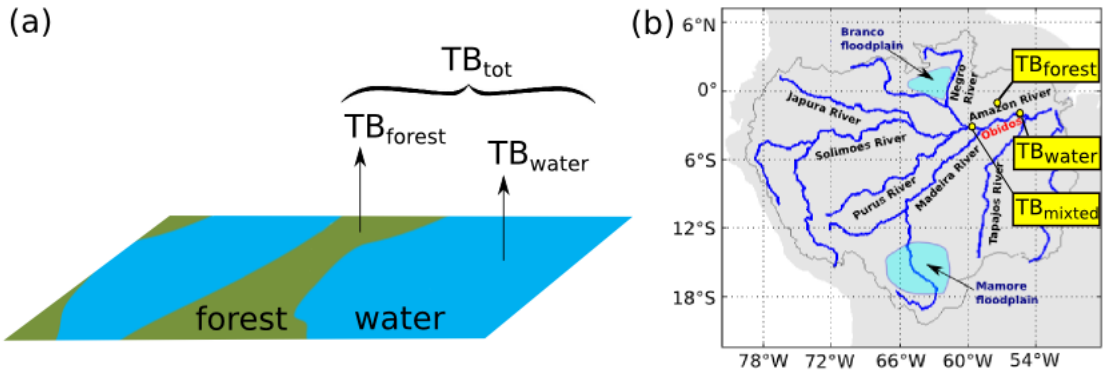

Figure 3. (**a**) Pixel representation with the two contributions: forest and water; (**b**) location of the "water", the "forest" and the mixed pixels.

Therefore, for a given pixel, the TB for the entire pixel is the sum of the water contribution and the forest contribution. The water contribution is the TB of the water weighted by the fraction of the pixel flooded, called the Surface WAterFraction (SWAF). In the same way, the contribution of the forest is the TB of the forest weighted by the part of the pixel not flooded (1-SWAF). The TB of the total pixel can be expressed as:

$$TB(\theta,p)_{tot} = SWAF(\theta,p)TB(\theta,p)_{water} + (1 - SWAF(\theta,p))TB(\theta,p)_{forest} \quad (1)$$

where θ is the incidence angle, p the polarization (p = H or V), $TB(\theta,p)_{tot}$ is the TB of the total pixel, $TB(\theta,p)_{water}$ the TB of the water and $TB(\theta,p)_{forest}$ the TB of the forest. The fraction of the water present in an SMOS pixel depends on both the incidence angle and the polarization and can be expressed as:

$$SWAF(\theta,p) = \frac{TB(\theta,p)_{tot} - TB(\theta,p)_{forest}}{TB(\theta,p)_{water} - TB(\theta,p)_{forest}} \quad (2)$$

$TB(\theta,p)_{tot}$ is the brightness temperature observed by the SMOS satellite. This observation is done over each pixel over the Amazon Basin. However, the $TB(\theta,p)_{forest}$ values are extracted over a selected pixel located at 2.137° S, 60.803° W (Figure 3) and composed exclusively of forest. The $TB(\theta,p)_{forest}$ are interpolated in time from the ascending SMOS overpass. In the same way, the $TB(\theta,p)_{water}$ time series are computed over a selected pixel located close to Obidos (2.142° S, 55.449° W) and composed of more than 80% water (Figure 3). Indeed, an SMOS pixel composed only of freshwater cannot been found (water from the ocean is salty, which modifies the emissivity). Therefore, the $TB(\theta,p)_{water}$ has been computed as the product of the emissivity and the skin temperature provided from the ECMWF. The Klein and Swift model [69] has been used to calculate the water emissivity. An average of the $TB(\theta,p)_{water}$ over the full period is computed to add more stability to the model. The $TB(\theta,p)_{water}$ is the only contribution that is constant in time in the model. Details about the value and the time series of both the $TB(\theta,p)_{forest}$ and $TB(\theta,p)_{water}$ are presented in the next section.
At this stage, an illustration is needed for a better comprehension of the algorithm. Figure 4 presents the time series of the $TB(\theta,p)_{water}$, $TB(\theta,p)_{forest}$ and a pixel annually flooded considered as "mixed" i.e., composed of both forest and water ($TB(\theta,p)_{mixed}$) located in Figure 3.

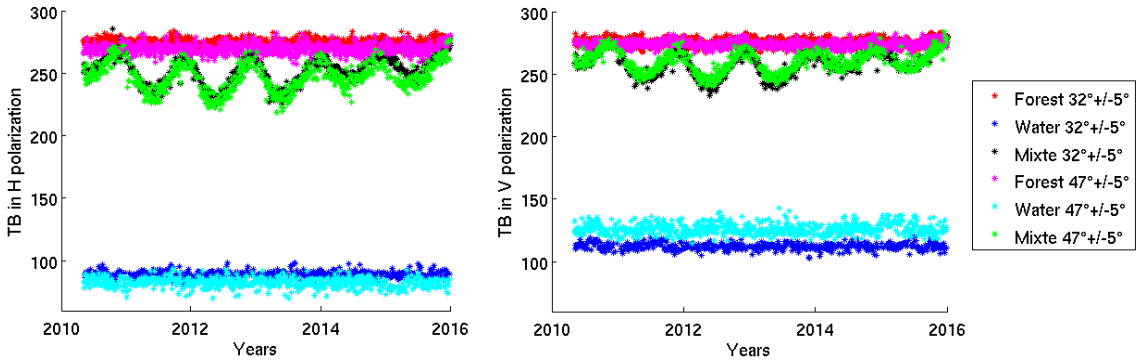

Figure 4. Time series of TB at H polarization (left) and V polarization (right) at two incidence angles (32°± 5° and 47°± 5°): the "water", "forest" and "mixed" pixels.

As shown in Figure 4, the $TB(\theta,p)$ values over the "forest", the "water" and the "mixed" pixels differ slightly following the angles and the polarization. For all of the polarization and the incidence angles, the $TB(\theta,p)$ values of the "water" pixel are the lowest, whereas the values of $TB(\theta,p)$ over the "forest" pixel are highest. The values of $TB(\theta,p)$ over the "mixed" pixel are included between the two contributions. Over the six years, the values of $TB(\theta,p)_{water}$ and $TB(\theta,p)_{forest}$ are very constant with time. This is not the case for the time series of $TB(\theta,p)_{mixed}$, which shows annual cycles due to the

annual inundation of the Amazon River. For the "mixed" pixel, at each date, Equation (2) is computed to obtain the SWAF value. This method is generalized over all of the pixels of the Amazon Basin (the localization of the "mixed" pixel moved, but the water and forest reference pixels are always the same). The $SWAF(\theta, p)$ data are computed each day with the SMOS ascending overpass and smoothed with a sliding window of 17 days.

The passive interferometric technique has some limitations over the areas with complex topography [70]. To avoid artifacts, SWAF data are not computed over areas with moderate topography according to the SMOS flag. Moreover, pixels with a topography index estimated as moderate or higher in the SMOS flag over the Amazon Basin were not considered.

4.1.2. Forest and Water TB Reference

As explained in the previous section, the time series of TB values over the "water" pixel are averaged in time to be sure of the $TB(\theta, p)_{water}$ stability. Results for each angle and polarization used in the algorithm are presented in Table 2. Lower values of TB are obtained in H polarization than in V polarization. In H polarization, the mean TB over the "water" pixel decreases with the increase of the incidence angles. The reverse is observed in V polarization. The signal over the "water" pixel is really stable during the full period as shown by the standard deviation, which does not exceed 1 K.

To compare the value obtained over the "water" pixel, the TB over the "forest" pixel are also averaged. However, note that these values are not used in the SWAF algorithm. For the "forest" pixel, the mean TB values increase for decreasing incidence angles, in both H and V polarization. This behavior is more marked in H polarization. The standard deviation of the TB over the "forest" pixel is higher than that observed over the "water" pixel, but does not exceed 4 K. Lower standard deviations are obtained in V polarization than in H polarization, except at $32^\circ \pm 5^\circ$.

Table 2. Average and standard deviation (σ) of the TB over the "water" and "forest" pixel in both H and V polarization and at four incidence angles ($32^\circ \pm 5^\circ$, $37^\circ \pm 5^\circ$, $42^\circ \pm 5^\circ$, $47^\circ \pm 5^\circ$).

	"Water" Pixel				"Forest" Pixel			
Incidence Angle	**H-pol**		**V-pol**		**H-pol**		**V-pol**	
	Mean (K)	σ (K)	Mean (K)	σ (K)	Mean (K)	σ (K)	Mean (K)	σ (K)
$32^\circ \pm 5^\circ$	94.52	0.51	122.58	0.64	274.43	2.71	276.61	2.72
$37^\circ \pm 5^\circ$	89.96	0.49	128.25	0.67	272.44	2.94	276.12	2.61
$42^\circ \pm 5^\circ$	84.72	0.46	135.27	0.70	271.88	3.57	275.72	2.71
$47^\circ \pm 5^\circ$	78.78	0.43	143.93	0.74	269.71	3.22	274.26	2.51

4.2. Statistic Scores' Computation

In this study, we use a common set of skill scores: (i) the coefficient of correlation (r); (ii) the p-value; (iii) the cross-correlation; (iv) the bias; and (v) the Root Mean Square Error (RMSE) value. The Pearson correlation coefficient (r) is used to compare the dynamic behavior of the SWAF data (x) with the dynamic evolution of other variables (y):

$$r = \frac{\sum_{i=1}^{n}(x_i - \overline{x})(y_i - \overline{y})}{\sqrt{(\sum_{i=1}^{n}(x_i - \overline{x})^2}\sqrt{(\sum_{i=1}^{n}(y_i - \overline{y})^2}} \quad \text{with} \quad \overline{x} = \frac{1}{n}\sum_{i=1}^{n} x_i \quad \text{and} \quad \overline{y} = \frac{1}{n}\sum_{i=1}^{n} y_i \tag{3}$$

with n the number of elements in the x and y series. Associated with the r, the p-value is also computed for the null hypothesis. The authors consider that for a p-value higher than 0.05, correlation values are not significant.

The cross-correlation measures the similarity of two time series (x and y) as a function of the displacement of one relative to the other. In this study, the displacement corresponds to the time (in months). Therefore, the cross-correlation value is the higher correlation value obtained if the x time

series is moved by n months with respect to the y time series.

The bias between two series (x and y) is defined as:

$$bias = \sum_{i=1}^{n} \frac{(x_i - y_i)}{n} \tag{4}$$

and the RMSE value is usually used to define the accuracy of the data. It is computed as:

$$RMSE = \sqrt{\frac{\sum_{i=1}^{n}(x_i - y_i)^2}{n}} \tag{5}$$

5. Results over the Amazon Basin

This section provides the SMOS water fraction results and analysis with a focus on the comparison and the validation of the product using a set of multi-source datasets described in Section 3.

5.1. Spatial Patterns and Temporal Dynamics of the SWAF Maps

This section described the spatial and temporal behavior of the water surface extent estimated by SMOS for the four angles and the two polarizations presented in Section 3.

Figure 5 shows the SMOS water fraction (SWAF) averaged over the 2010–2015 period for the entire Amazon Basin. Results are presented for four angle bins: ($32^\circ \pm 5^\circ$, $37^\circ \pm 5^\circ$, $42^\circ \pm 5^\circ$, $47^\circ \pm 5^\circ$) and the two polarizations (H and V pol). From Figure 5, it can be seen that independent of the incidence angles and polarizations, the major spatial patterns of the Amazon Basin are observed: the Amazon River and its tributaries, the Mamore floodplain in the south of the basin, the Branco floodplain in the north of the basin and the Balbina lake located in the north of Manaus. For a given angle, the spatial distribution of the SWAF is close in H and V polarization. However, the percentage of water fraction estimate is slightly higher at H polarization than V polarization. The major difference concerns the spatial distribution of the SWAF sensed at low incidence angle ($32^\circ \pm 5^\circ$) and at high incidence angle ($47^\circ \pm 5^\circ$). Low incidence angles reveal small patterns of SWAF and, in particular, the smaller Amazon River west affluent. Conversely, SWAF sensed with a higher incidence angle shows only the major structure of the flooded areas (Amazon River, Rio Negro River, Mamore plain, etc.).

Figure 6 shows the temporal dynamic of the SWAF for the full basin for the eight SMOS configurations. For all of the angles and the polarizations, water surface extent exhibits a clear seasonal cycle. The minimum of the inundation is observed in March, whereas the maximum of the flooding is reached during October. This observation is valid for all of the angles and polarization. Both in H and V polarization, for all of the incidence angles, the temporal dynamics of the SWAF are in good agreement, except for the incidence angle of $47^\circ \pm 5^\circ$. SWAF sensed with the highest incidence angle underestimates the water fraction in the Amazon Basin with respect to lower angles. In V polarization, on average, the Amazon Basin is less flooded than in H polarization. These results are in accordance with Figure 5. During the wet season, almost 1% of the Amazon Basin is flooded, whereas during the dry season, only 0.2% of the basin is flooded.

Figure 7 shows the monthly spatial variability of the SWAF product over the Amazon Basin. The monthly average has been computed during the full period (2010–2015) at V-polarization and at $32^\circ \pm 5^\circ$ of incidence angle. The Amazon River, its main tributaries and the major floodplains are well represented for all of the months. The maximum of the inundation of the Amazon River is observed between March and July. The spatial and temporal variation of the Mamore floodplain is well described by the SWAF data. This floodplain is inundated from January–June, and the least flooding is observed during September and October. The major Amazon tributaries are more flooded between January and May. Similar results are observed at H polarization and higher incidence angles (not shown).

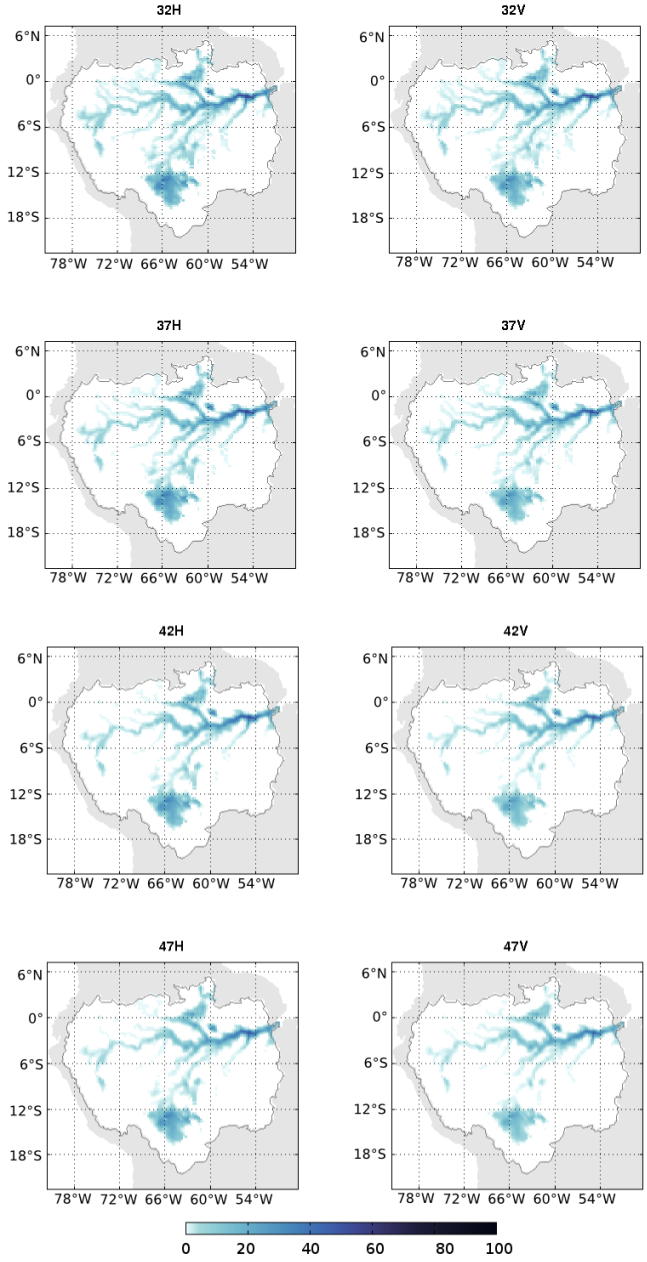

Figure 5. Average in time of the SMOS water fraction during 2010–2015 over the full Amazon Basin. Both H and V polarization and the four incidence angles (32°± 5°, 37°± 5°, 42°± 5°, 47°± 5°) are considered.

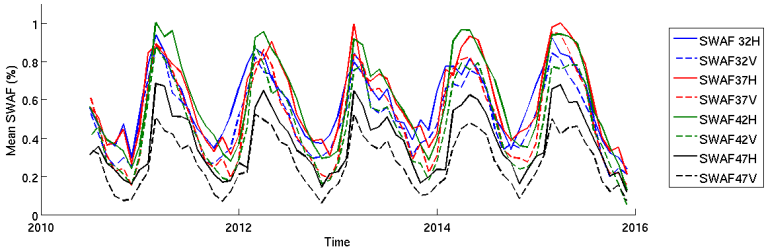

Figure 6. Spatial average of the SWAF over the full Amazon Basin in H polarization (lines) and V polarization (dashed lines) for the four incidence angles: 32°± 5° (blue), 37°± 5° (red), 42°± 5° (green) and 47°± 5° (black).

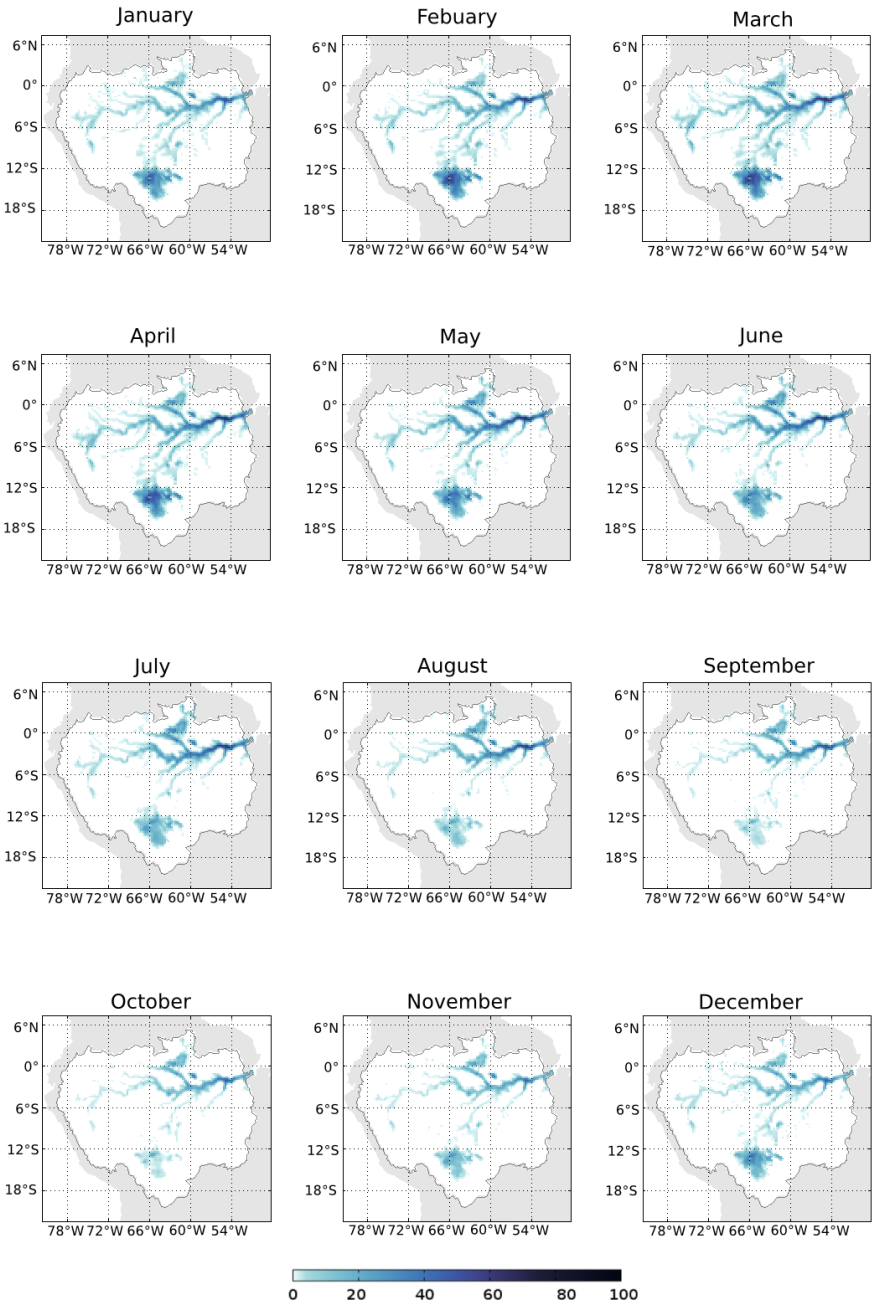

Figure 7. Monthly average of the SWAF product from 2010–2015 at V-polarization and at 32° ± 5° incidence angle.

5.2. Comparison and Validation

In the following section, the SWAF product is compared to other data sources and variables: static and dynamic water extent maps, water level measured by altimetry satellite, in situ river discharge at the outlet of the basin and precipitation data. The static land surface maps obtained by optical sensors and the GIEMS product were also used to analyze the spatial patterns. The SWAF data were also compared to the dynamic water fraction product available over the Amazon Basin, the SWAMPS product. Note that all of these datasets are completely independent from the SMOS water surface extent maps.

5.2.1. Comparison to Static and Climatological Water Extent Maps

The SWAF temporal average over the entire Amazon Basin had been compared to three static land cover maps (IGBP [62], GlobeCover [63] and ESA CCI [64]) and the mean of the GIEMS water fraction maps. These maps are detailed in Section 3.5 and presented in Figure 2. Main similar patterns can be observed from the three different static land cover maps. The number of pixels partially flooded over the Amazon Basin is higher for the GlobeCover map than for both the IGBP and ESA CCI maps. Conversely, the ESA CCI map produces less pixels totally flooded over the Amazon Basin than the others maps. IGBP, GlobeCover and ESA CCI maps present inundation surfaces of 220,000 km^2, 360,000 km^2 and 210,000 km^2, respectively. Note that the static maps are based on data from different time periods (see Section 3.5), and the inland water occupation can change with time and anthropogenic activities.

The average GIEMS product over the 1993–2007 period is presented in Figure 2. The Amazon River, its major tributaries, southern and northern floodplains are well depicted. On average, over the 1993–2007 period, 440,000 km^2 of the surface were flooded.

Figure 8 presents the mean distribution (2010–2015) of the water fraction extent for the IGBP map, GlobeCover map, ESA CCI map, GIEMS averaging and the temporal average of all of the SWAF products for the eight SMOS configurations over the Amazon Basin. For all of the products, the majority of the pixels are partly flooded, and a few of them are totally flooded. The distributions of both IGBP and ESA CCI are very close. The GlobeCover map and the mean GIEMS product (1993–2007) provide larger estimates of pixels flooded or partially flooded with respect to the other products, in particular for water fraction higher than 0.4. For all of the SMOS configurations, the distributions of the SWAF products are comprised between both the GlobeCover and GIEMS distributions and both the IGBP and ESA CCI distributions. Between the eight SMOS configurations, only a few differences in their spatial distributions can be noticed. Both in H and V polarizations, a decrease of the incidence angle leads to a decrease of the detection of pixels partially flooded. In V polarization, fewer pixels are flooded than in H polarization. This behavior is particularly marked for water fraction ranges between 10% and 40%. This trend makes the SWAF computed in V polarization closer to the IGBP and ESA CCI maps than the SWAF calculated in H polarization for the moderately flooded pixels. Table 3 presents an average of the number of square kilometers flooded in the Amazon Basin. Figures 5 and 8 and Table 3 confirm that, on average, the number of square kilometers flooded decreases for increasing incidence angles, and more flooded areas are detected in H polarization than in V polarization. Independent of the selected SMOS configuration, the number of square kilometers flooded is in the range between the IGBP and GlobeCover estimates.

Figure 9 presents the bias (reference static maps, SWAF configurations) and the RMSE between water surface extent for each reference maps used in Figure 8 and the water surface extent for the eight SMOS configurations. For all of the SWAF configurations, lower bias is obtained by comparing the SWAF data with IGBP (mean bias = 0.6%) and ESA CCI (mean bias = −0.4%). Higher bias is obtained by comparing SWAF data with the GlobeCover map (mean bias = 5.9%). Bias between the static maps and the SWAF data is always higher at V-polarization than at H-polarization for all of the static maps. Moreover, the bias values increase with the growth of the incidence angles. A lower RMSE value is obtained by comparing the SWAF data with the ESA CCI map (mean RMSE = 5.8%), and a higher RMSE value is obtained with the GlobeCover map (mean RMSE = 17.8%). Following the static map considered, the behavior of the SWAF data with respect to angles and polarization differs. For IGBP and ESA CCI maps, lower values of RMSE are obtained at V-polarization than at H-polarization, and a slight decrease of the RMSE values is observed with the increase of the incidence angles. The contrary is noticed for the comparison with the GIEMS data. No trend concerning the RMSE behavior is observed for the comparison between the SWAF data and the GlobeCover data.

Table 3. Average of the number of square kilometers flooded in the Amazon Basin for the eight SMOS configurations.

Incidence Angle (°)	H-pol	V-pol
$32° \pm 5°$	290,000	270,000
$37° \pm 5°$	280,000	260,000
$42° \pm 5°$	280,000	250,000
$47° \pm 5°$	280,000	250,000

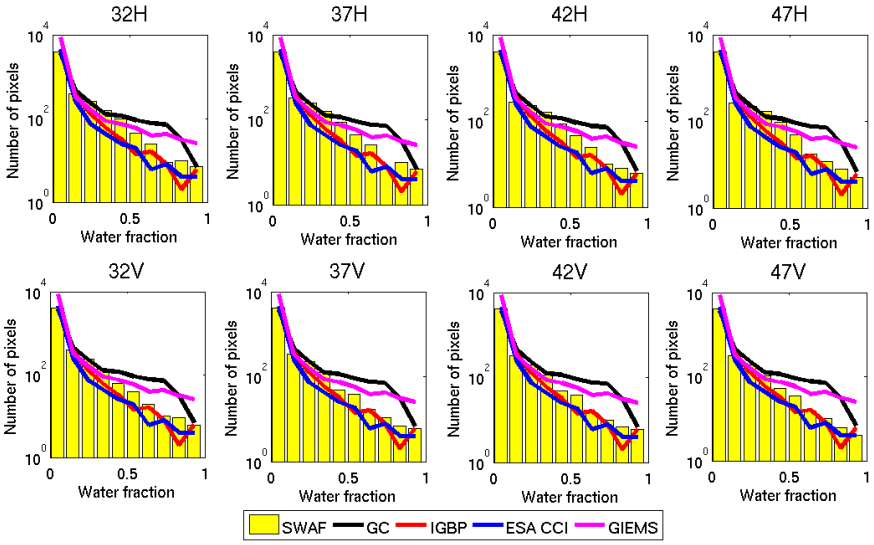

Figure 8. Histogram of water fraction for the IGBP map (red), GlobeCover map (black), the ESA CCI (blue) and SWAF (yellow columns) for eight SMOS TB configurations (32–47 angle bins and H/V configurations).

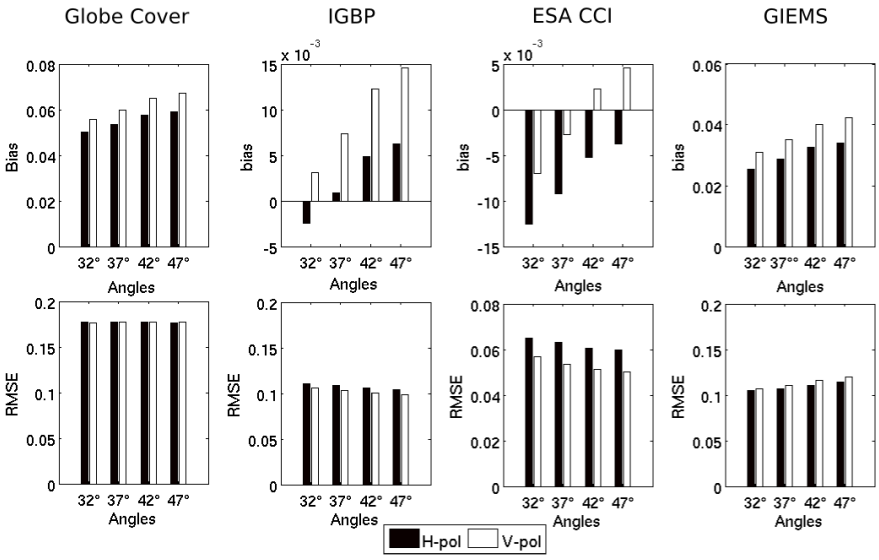

Figure 9. Bias (reference static maps, SWAF) and RMSE values computed between each reference maps (GlobeCover, IGBP, ESA CCI, GIEMS) and SWAF for the eight configurations.

5.2.2. Comparison with Water Height Measured by Altimetry

For low topography slopes, the water surface extent can be related to the water height. Other studies [32,66] had already shown that the seasonal and inter-annual variation patterns of

the surface water extent and the water level agree well. In this present study, the water levels measured by the Jason-2 satellite were compared with the SWAF product over 83 virtual stations during the 2010–2012 periods. Results are presented in Figure 10. Only stations with significant results (p-value < 0.01) are represented. The color dot indicates the correlation value for each virtual station. The gray color dots show the virtual station with non-significant results. For all of the SMOS configurations, the correlation value between the water fraction and the water level measured by Jason-2 is very high ($r > 0.8$) throughout the Amazon River and the major tributaries. The lower correlation values are located over areas where the relation between the water surface's extent and the water level is not direct. For a given angle, slight differences in terms of correlation values are observed with respect to the polarization choice. The number of not significant stations varies following angles and polarization. At H polarization, the number of no significant stations is equal to 36, 33, 33 and 44 for angles from $32^\circ \pm 5^\circ$–$47^\circ \pm 5^\circ$, respectively. At V-polarization, the number of no significant stations is slightly lower and equal to: 35, 30, 31 and 44, respectively.

To formalize this information, the sum of the correlation values for each SMOS configuration is presented in Figure 11. Only stations with significant correlations for the eight SMOS configuration are considered to compute this figure. The sum of the correlation values between the SWAF and the water level estimated by altimetry is always higher at V-polarization than at H-polarization, except at $32^\circ \pm 5^\circ$. The higher sum of correlation is obtained at V polarization and at $47^\circ \pm 5^\circ$ incidence angle. At high incidence angles, higher correlation values are obtained, but the number of significant stations is lower. The contrary is observed at low incidence angles.

5.2.3. Comparison with SWAMPS Dynamic Surface Extent

The recent SWAMPS product provides a daily estimation of the surface water extent. Note that the SWAMPS products are obtained by more complex algorithm merging active and passive microwaves than the SWAF data. Figure 2 shows the average of the SWAMPS water fraction over the Amazon Basin from January 2010–March 2013. Spatially, the mean SWAF and SWAMPS products are in good agreement. Both in the SWAF and SWAMPS products, the Amazon River and its tributaries are well represented, and the major floodplains are present. In the SWAF data, no data are provided over the southeast part of the Amazon Basin due to high topographic index where as the SWAMPS product shows some patterns of water surface over the same region. An important difference between the two products is the spread of the rivers. In the SWAMPS product, all of the rivers have a larger floodplain area than in the SWAF data. Over the two major floodplains of the Amazon Basin, different patterns are observed in the SWAF data. This behavior is not observed for the SWAMPS data. The water surface extents estimated by the SWAMPS data are lower than those estimated by the SWAF data.

Figure 12 shows the temporal correlation values between the SWAMPS and SWAF data from January 2010–March 2013 for all of the SMOS configurations. The correlation value is computed only over pixels where both SWAMPS and SWAF water fraction are present. For all of the SMOS configurations, a good agreement ($r > 0.8$) between the SWAF and SWAMPS products is observed over the Amazon River and the two largest floodplains of the basin. Over these locations, the temporal dynamics of the surface water are well described by the two products. Concerning the Amazon tributaries, results are more contrasting, and the SWAF and the SWAMPS seem to have a different temporal dynamics. In terms of SMOS configurations, results are very similar whatever the incidence angle and polarization chosen. For example, the number of pixels that obtained a high correlation value ($r > 0.8$) between the SWAF and the SWAMPS products ranges between 147 (for $32^\circ \pm 5^\circ$ in H-pol) and 172 (for $47^\circ \pm 5^\circ$ in H-pol). No trend is noticed between high and low angles or V and H polarization. For the accepted correlation value ($r > 0.6$), the number of pixels that satisfied these criteria ranges between 1097 (for $47^\circ \pm 5^\circ$ in V-pol) and 1247 (for $37^\circ \pm 5^\circ$ in V-pol). In this case, a clear trend is observed: increasing the incidence angle leads to decreasing the number of pixels with an accepted correlation.

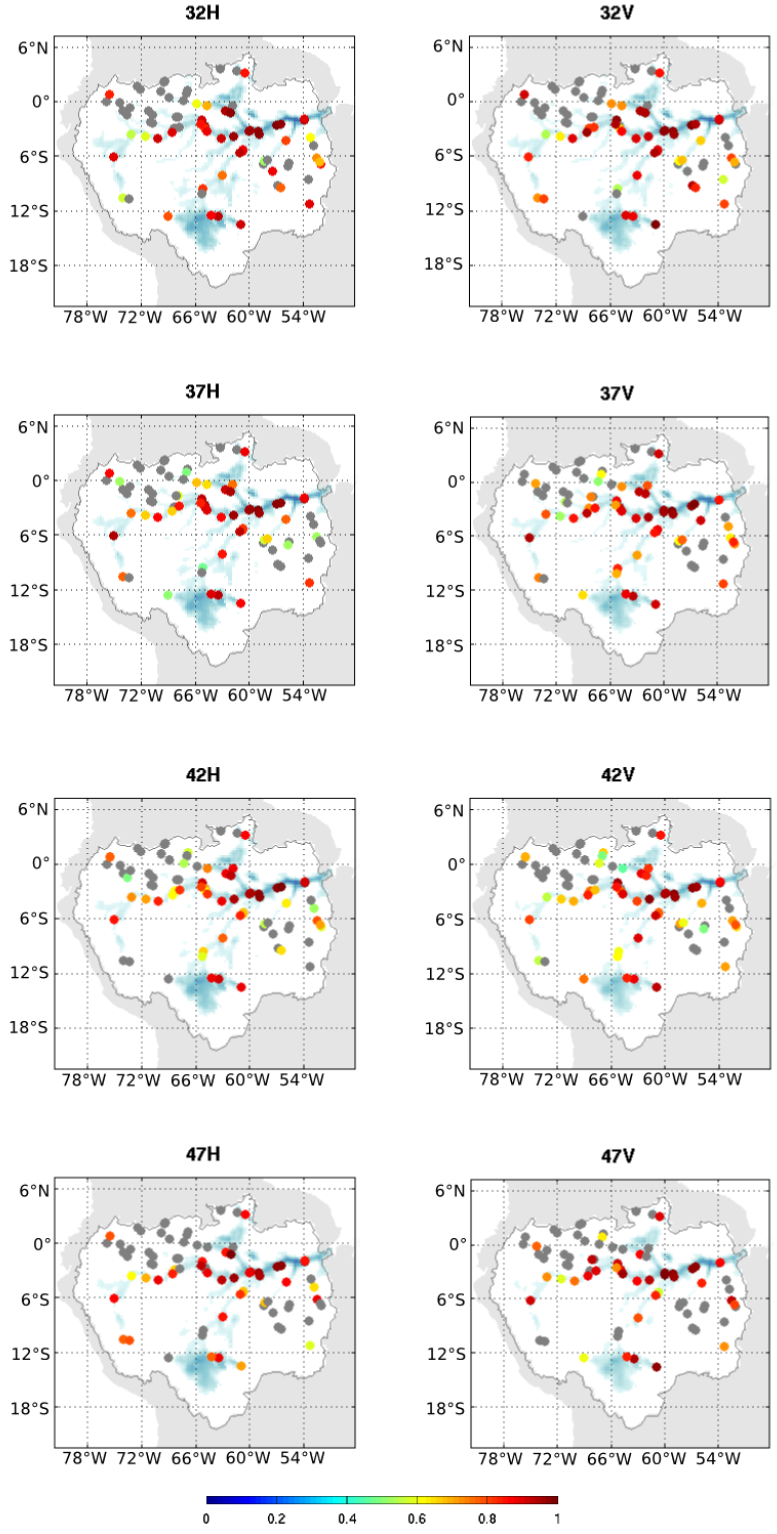

Figure 10. For each SMOS configuration, correlation values against the SWAF water surface extent and the water level measured by Jason-2 during 2010–2012. The color dot represents the correlation value. Gray color dots show no significant results (p-value > 0.05).

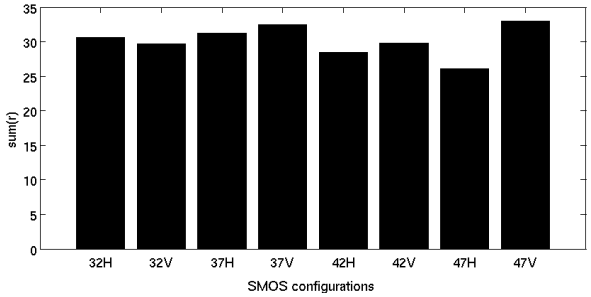

Figure 11. For each SMOS configuration, the sum of the correlation value (r) obtained in Figure 8. Only significant stations for all of the SMOS configuration are used for the computation.

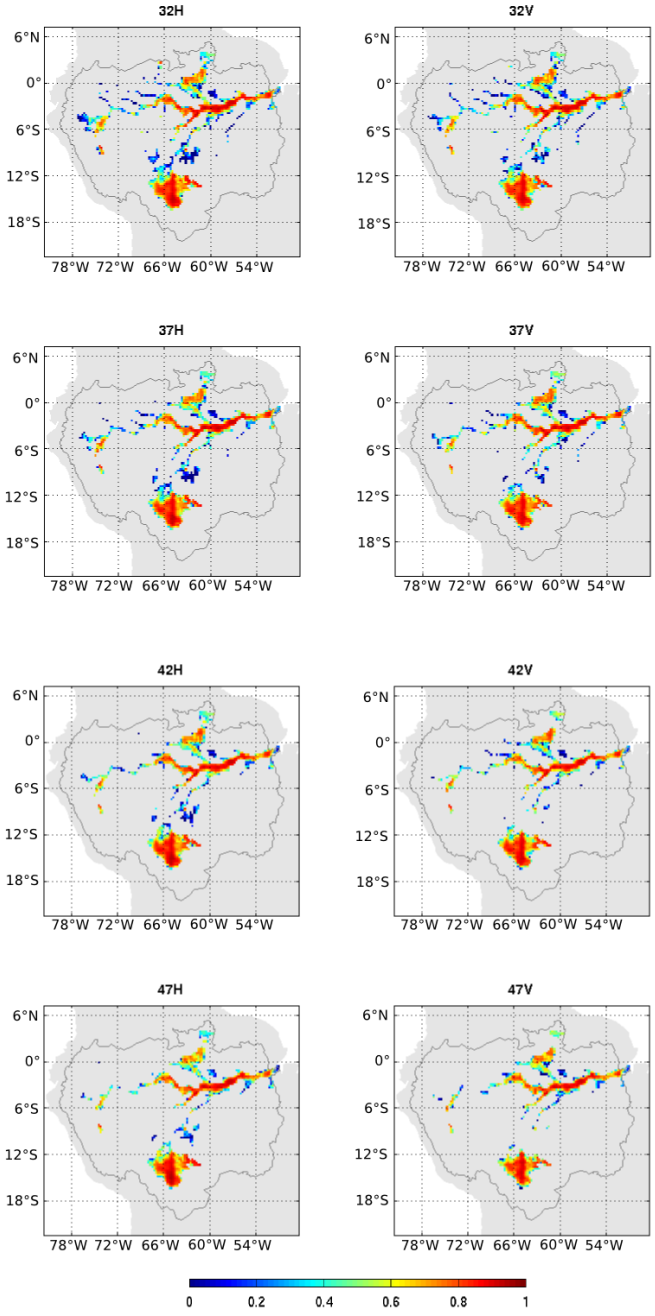

Figure 12. Temporal correlation values between the SWAMPS and SWAF products from January 2010–March 2013 for each SMOS configuration.

5.2.4. Link between SWAF and the Hydrological Components

Strong seasonal and interannual variations can be observed in both precipitation and surface water extent in the Amazon Basin. Figure 13 presents the standardized anomalies (i.e., the time series of a hydrological parameter minus the average of the time series divided by its standard deviation of the observation period) of both precipitation from TRMM and SWAF products for the eight SMOS configurations over the entire Amazon Basin. Note that inundation is highly linked to the precipitation events, but can also occur in response to snow melt or heavy precipitation at upstream locations. In this case, flooded areas and precipitation are separated in both time and space. A good agreement between all of the SWAF products whatever the polarization or the incidence angles can be noticed, except at 47°± 5° in H polarization. For the entire Amazon Basin, the cross-correlation values between the TRMM precipitation and the SWAF products are shown in Table 4. The best correlation values are obtained at 42° ± 5° and 32° ± 5°. In H and V polarization, similar correlation values were obtained. The correlation value is highly impacted by the choice of the incidence angle, whereas the polarization plays a negligible role. Note that using the angle 47° ± 5° strongly degrades the correlation value between the precipitation and the water surface extent. By computing the time lag correlation values, a time lag of two months was found between the precipitations and the water surface for all of the SMOS configurations, except for the angle of 47° ± 5° (four months).

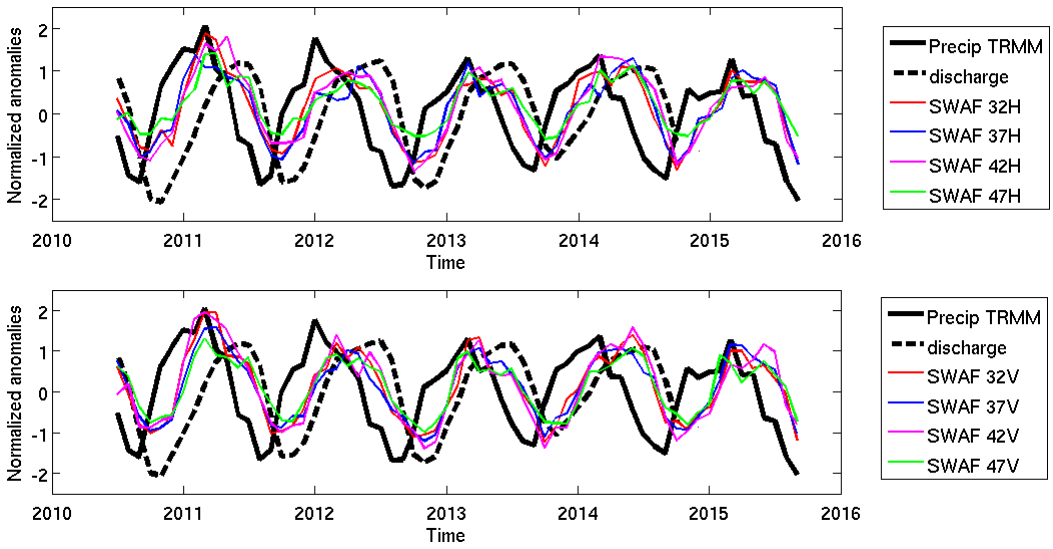

Figure 13. Monthly normalized anomalies of precipitation (TRMM data), in situ discharge at Obidos and the SWAF at H-pol (top) and V-pol (bottom) with the four incidence angles considered in this study. The precipitation and SWAF anomalies were computed over the entire Amazon Basin.

The time series of the Amazon River discharge is closely linked to the total amount of the surface water extent in the whole basin [43]. Figure 13 also shows the monthly normalized anomalies of the in situ river discharge measured at Obidos. By computing the time lag correlation values, it was found that the maximum water surface extent often precedes the maximum Amazon discharge. For the entire Amazon Basin, the cross-correlation values between the in situ discharge at Obidos and the SWAF products are reported in the Table 4. High cross-correlation values are obtained between the discharge and all of the SWAF products varying from 0.78 (47° ± 5 ° at H-pol) to 0.88 (42° ± 5° at H-pol). For all of the SWAF configurations, the maximum water surface extent precedes the discharge by one month. The normalized anomalies of SWAF whatever the SMOS configuration are better correlated with the normalized anomalies of discharge than those of precipitation. The cross-correlation value between the normalized anomalies of precipitation and discharge is equal to 0.84 with a time lag of four months for the whole Amazon Basin.

Table 4. Cross-correlation (r) values between TRMM precipitation, discharge at the outlet and the SWAF products for the eight configurations over the 2010–2015 period.

	Precipitation		Discharge	
Incidence Angle (°)	**H-pol**	**V-pol**	**H-pol**	**V-pol**
$32° \pm 5°$	0.91	0.90	0.83	0.84
$37° \pm 5°$	0.88	0.89	0.86	0.85
$42° \pm 5°$	0.92	0.88	0.88	0.82
$47° \pm 5°$	0.83	0.85	0.78	0.83

6. Discussion

6.1. Water Surface Validation

The SWAF products and the aggregated high spatial resolution of the IGBP and ESA CCI maps over the Amazon Basin showed a good agreement (see Figures 8 and 9). The mean bias and RMSE between the SWAF for all of the configurations and the IGBP map is equal to 0.6% and 10%, respectively. Better results are obtained for the comparison of the SWAF and the ESA CCI maps (mean bias = −0.4% and mean RMSE = 5.8%). The SWAF sensitivity to seasonal and annual water fraction extent was also demonstrated in the comparison against precipitation and discharge dynamics. The comparison between the anomaly of water surface dynamics estimated from the SWAF products over the entire Amazon Basin and the anomaly of discharge at the mouth of the Amazon showed a shift of one month. This result is in good agreement with previous research papers. For example, results presenting the same time-lag for surface water extent [43], surface water storage [49] and terrestrial water storage [71]. Our findings showed that precipitation often preceded the water surface dynamic by two months over the Amazon Basin. These results also agree well with previous studies [43,71].

6.2. Impact of the Angles and Polarization on the Water Surface Retrievals

The SMOS mission provides data in multi-angular and full polarization modes. A specific analysis is presented to determine the best acquisition configuration to retrieve the water fraction from SMOS. The use of combined polarization and angles was used in this study as the single angle and channel gave satisfactory results. As shown in the previous section, the spatio-temporal evolution of the SWAF estimated using different angles and polarizations was very close in the Amazon Basin. Differences are mainly present in areas far from the main Amazon river stream characterized by high vegetation density. Table 5 summaries the best SMOS configurations (low or high incidence angles and H or V polarizations) in order to obtain the higher agreement between the SWAF product and each variable used for validation (land cover classification, water level, dynamic water fraction, precipitation and discharge). "NS" stands for Non-Significant, and it is used when no trend in the results (see previous section) was observed.

Table 5. Summary of the best SMOS configurations permitting a good agreement between SWAF and the other variables. Green color means that good agreement was found, whereas the red color means the opposite. See Section 5 for the results. NS, Non-Significant.

Variables	**H-pol**	**V-pol**	**Low angles**	**High angles**
Land cover classification			NS	NS
Water level			NS	NS
Dynamic water fraction	NS	NS		
Precipitation	NS	NS	NS	NS
Discharge	NS	NS	NS	NS

Table 5 shows that the low incidence angles were more suitable to detect the dynamic water surface extent over the tropical regions. This result was expected based on the microwave signal theory [72]. The H-polarization tends to overestimate the water fraction extent for a low fraction

(<50%). Over the Amazon Basin, low incidence angles at V polarization are the best configuration to compute the water fraction extent with the SMOS data. For future studies, the authors advise to use the SWAF products at low incidence angles and at V polarization over tropical areas. In the near future, SWAF estimated in both H and V polarization at low incidence angle will be combined to extend the domain of applicability of the algorithm to other environments to increase the water sensibility to the SWAF product.

6.3. Impact of Vegetation Cover

Estimating water surface extent under dense vegetation with passive microwave is challenging. The work in [26,27] provided estimates of the water surface extent over the Amazon Basin by using the passive microwave SMMR sensor at 37 GHz (Q-band). They found good agreement in the seasonal changes in inundation area and good correlations values with the water level in Manaus. However, they noticed the effects of the vegetation on their results, in particular for small patches of open water intermixed with vegetation canopies or from an attenuating effect of homogeneous canopies overlying water surfaces. To overcome the vegetation attenuation, the GIEMS product mixed passive and active microwave products at coarse spatial resolution with the optical dataset at finer resolution, which enhances the capability to detect the small water fraction. However, this capability could be hampering over dense vegetated area and frequently cloud-covered regions, such as the tropical ones, due to the limitation of the optical sensors. The frequencies of the passive microwave data from SSM/I are at 19 GHz (K band) and 85 GHz (E band), and the active one is at 5.25 GHz (C band). The work in [34] showed that the low frequencies were less sensitive to the vegetation effects than the higher frequency. The results presented in this study are the first to demonstrate the potential of L-band (1.4 GHz) brightness temperature to estimate surface water extent under dense vegetation.

6.4. Limitations and Prospects of the SWAF Dataset

The most important limitation of the SWAF product is its coarse resolution inherent to the passive microwave sensor. This limitation was already noticed for the GIEMS [42] products using microwave sensors. This limitation implies that the water surface lower than 4% for all of the angles and polarization could not be mapped by the SWAF products.

The SMOS sensor is based on dual polarizations and multi-angular measurements. Mountainous areas modify local incidence angles and multi-scattering, which impacts the TB values [70] and, consequently, the water surface estimation. The effects led to an overestimation of the water fraction. To overcome this effect, areas with moderate to strong topographic slopes were not considered in this study.

The snow is also an important component of the hydrological cycle. Due to the impact of the topography slopes on the TB and the presence of the snow only over the mountainous areas in the tropical basins, the temporal evolution of the snow coverage from the Andes Mountains has not been investigated in this study.

The method developed in this study is based on the impact of surface water at the L-band signal and based on the stability over time of the TB measured over dense forests. Some additional computation was performed to measure the sensitivity of the SWAF product to the "forest" reference point. It was found that instead of choosing only one reference "forest" pixel, but a set of pixels composed only of forest, the mean TB increases by 3 K for all of the incidence angles and polarization. This value is included in the incertitude range. However, this growth on the TB "forest" reference value tends to increase the SWAF by 8%. Concerning the "water" reference point, no change was observed by choosing a set of pure water pixels. Moreover, the method applied in this study could not be applied in areas where the TB over vegetation is not stable over time or not dense enough. Future work will concentrate on the extension of the current algorithm to other environments by using multi-angular information. By solving this limitation, the water fraction would be estimated at the global scale by using only one dataset and a simple approach.

7. Conclusions and Prospect

This study presents the validation and the link to other hydrological components of regional (Amazon Basin) daily and multi-year (2010–2015) water surface extent maps from the SMOS mission at coarse resolution (25 km $\times$ 25 km). The SWAF product is based on L-band acquisitions. At such a frequency, the signal is highly sensitive to the standing water above the ground, and it is expected to penetrate deeper in the vegetation than at higher frequencies, such as visible and infrared or microwave at higher frequencies. As the L-band signal is more sensitive to open water under dense vegetation, the SWAF product provides surface water extent estimates (percentage of inundation in a pixel of 25 $\times$ 25 km) with a high temporal resolution ($<$3 days) based on the accumulation of daily surface water extent in the Amazon Basin between 2010 and 2015. The SWAF product is computed from the L-band, and it can be computed easily and quickly without any ancillary data. Over this basin, the water surface extent showed a strong seasonal and interannual variability with two marked droughts in 2010 and 2015.

The SWAF data were compared to three sets of static land cover maps provided from visible sensors (IGBP, GlobeCover and ESA CCI) and the average inundation extent from GIEMS over 1993–2007. It was found that the SWAF products are close to the IGBP and ESA CCI maps. On average and during the 2010–2015 period, 270,000 km^2 were inundated over the Amazon Basin. A slight overestimation of the flooded areas could be noticed. Over the Amazon Basin, the SWAF products were highly correlated with water levels measured by Jason-2 ($r > 0.8$) for the significant stations. The temporal dynamics of the SWAF products were also validated against precipitation (TRMM data) and in situ discharge at the mouth of each river. It was found that over the Amazon Basin, the precipitations often precede the inundation by three months, and the water surface extent impacts the discharge at the mouth of the Amazon after one month. As expected by the microwave theory, the mall water fraction could not be detected by the large footprint of SMOS. This implied that low water fraction extent ($<$4%) could not be mapped by the SWAF products. The mountainous areas were also a limitation of the SWAF products. The topography-modified local incidence angles implied significant impact on the microwave signal and, consequently, on the water surface estimation. The effects led to overestimation of the water fraction. To avoid this effect, the areas with high topography slopes were flagged in the SWAF products.

Based on the SMOS product, the SWAF products declined with several incidence angles at two polarizations (H and V). It was clear that high incidence angles ($>47^\circ \pm 5^\circ$) were not suitable to sense the water surface from the L-band microwave signal. The H-polarization tended to increase the lower value of the water fraction extent with respect to the V-polarization. The SWAF products computed with different angles and polarizations led to similar results with very slight differences over the Amazon Basin. For future use, the authors advise the use of SWAF computed with low incidence angles ($32^\circ \pm 5^\circ$ and/or $37^\circ \pm 5^\circ$) at V for the Amazon Basin.

The methodology permitting retrieval of the water fraction applied in this study does not require much computation time and can be easily be applied to another L- band microwave dataset, such as the new Soil Moisture Active and Passive (SMAP) data or an older dataset (SSM/I...). The method had been validated over the Amazon Basin by taking advantage of the numerous data and research performed over this area.

In the near future, this recent water surface fraction product can be easily extended with the future SMOS data and the Soil Moisture Active and Passive (SMAP) data to obtain a long record of inundation products under dense vegetation. These data will be useful to better understand the water, carbon and methane cycles over the tropical areas. By adding a third component (saturated soil) on the first-order radiative transfer, this method is likely to be applied in other regions in the world.

Acknowledgments: This work was funded by the program Terre Océan Surfaces Continentales et Atmosphère (TOSCA, France) and the CNES under the project TOSCA-SOLE and Marie Parrens was funded by the CNES PostDoc program.

Author Contributions: Ahmad Al Bitar and Marie Parrens conceived of and designed the algorithms. Marie Parrens performed the analysis. Frédéric Frappart has contributed to the evaluation of the products. Frédéric Frappart, Fabrice Papa, Jean-François Crétaux and Stephane Calmant, Jean-Pierre Wigneron and Yann Kerr provided scientific expertise, datasets and corrections to the manuscript. Marie Parrens and Ahmad Al Bitar wrote the manuscript with contributions from all of the co-authors.

Conflicts of Interest: The authors declare no conflict of interest. The founding sponsors had no role in the design of the study; in the collection, analyses or interpretation of data; in the writing of the manuscript; nor in the decision to publish the results.

Abbreviations

The following abbreviations are used in this manuscript:

SAR	Synthetic Aperture Radar
SWOT	Surface Water Ocean Topography
V	Vertical
H	Horizontal
SMMR	Scanning Multichannel Microwave Radiometer
GIEMS	Global Inundation Extent from Multi-Satellites
SSMI/I	Special Sensor Microwave/Imager
ERS	European Remote Sensing
QSAT	QuickSCAT
ASCAT	Advanced Scatterometer
SSM/S	Special Sensor Microwave/Sounder
SMOS	Soil Moisture and Ocean Salinity
SMAP	Soil Moisture Active and Passive
ESA	European Space Agency
CNES	Centre National d'Etude Spatiale
CDTI	Centro para el Desarrollo Teccnologico Industrial
L	Level
EASE	Equal-Area Scalable Earth
SRTM	Shuttle Radar Topography Mission
USGS	U.S. Geological Survey
IGBP	International Geosphere Biosphere Programme
AVHRR	Advanced Very High Resolution Radiometer
MODIS	Moderate Resolution Imaging Spectroradiometer
CCI	Climate Change Initiative
NASA	North America Space Agency
TRMM	Tropical Rainfall Measuring Mission
ECMWF	European Center for Medium range Weather Forecasting
SWAF	SMOS WAter Fraction
ENVISAT	ENVironment SATellite
TB	Brightness Temperature

References

1. Matthews, E.; Fung, I. Methane emission from natural wetlands: Global distribution, area, and environmental characteristics of sources. *Glob. Biogeochem. Cycles* **1987**, *1*, 61–86.
2. Mitsch, W.; Gosselink, J. *Wetlands*, 3rd ed.; John Wiley & Sons, Inc.: Hoboken, NJ, USA, 2000.
3. Cole, J.J.; Prairie, Y.T.; Caraco, N.F.; McDowell, W.H.; Tranvik, L.J.; Striegl, R.G.; Duarte, C.M.; Kortelainen, P.; Downing, J.A.; Middelburg, J.J.; et al. Plumbing the global carbon cycle: Integrating inland waters into the terrestrial carbon budget. *Ecosystems* **2007**, *10*, 172–185.
4. Sjögersten, S.; Black, C.R.; Evers, S.; Hoyos-Santillan, J.; Wright, E.L.; Turner, B.L. Tropical wetlands: A missing link in the global carbon cycle? *Glob. Biogeochem. Cycles* **2014**, *28*, 1371–1386.
5. Alsdorf, D.E.; Rodriguez, E.; Lettenmaier, D.P. Measuring surface water from space. *Rev. Geophys.* **2007**, *45*, doi:10.1029/2006RG000197.

6. Bakker, K. Water security: Research challenges and opportunities. *Science* **2012**, *337*, 914–915.
7. Finlayson, C.; Davidson, N. *Global Review of Wetland Resources and Priorities for Wetland Inventory*; Preface iv Summary Report; CM Finlayson & AG Spiers: Canberra, CT, USA, 1999; p. 15.
8. Vörösmarty, C.; Hoekstra, A.; Bunn, S.; Conway, D.; Gupta, J. Fresh water goes global. *Science* **2015**, *349*, 478–479.
9. Costanza, R.; de Groot, R.; Sutton, P.; van der Ploeg, S.; Anderson, S.J.; Kubiszewski, I.; Farber, S.; Turner, R.K. Changes in the global value of ecosystem services. *Glob. Environ. Chang.* **2014**, *26*, 152–158.
10. Pekel, J.F.; Cottam, A.; Gorelick, N.; Belward, A.S. High-resolution mapping of global surface water and its long-term changes. *Nature* **2016**, *540*, 418–422.
11. Smith, L.C. Satellite remote sensing of river inundation area, stage, and discharge: A review. *Hydrol. Process.* **1997**, *11*, 1427–1439.
12. Frazier, P.S.; Page, K.J. Water body detection and delineation with Landsat TM data. *Photogramm. Eng. Remote Sens.* **2000**, *66*, 1461–1468.
13. Verpoorter, C.; Kutser, T.; Seekell, D.A.; Tranvik, L.J. A global inventory of lakes based on high-resolution satellite imagery. *Geophys. Res. Lett.* **2014**, *41*, 6396–6402.
14. Feng, M.; Sexton, J.O.; Channan, S.; Townshend, J.R. A global, high-resolution (30-m) inland water body dataset for 2000: First results of a topographic–spectral classification algorithm. *Int. J. Digit. Earth* **2016**, *9*, 113–133.
15. Crétaux, J.F.; Jelinski, W.; Calmant, S.; Kouraev, A.; Vuglinski, V.; Bergé-Nguyen, M.; Gennero, M.C.; Nino, F.; Del Rio, R.A.; Cazenave, A.; et al. SOLS: A lake database to monitor in the Near Real Time water level and storage variations from remote sensing data. *Adv. Space Res.* **2011**, *47*, 1497–1507.
16. Frappart, F.; Do Minh, K.; L'Hermitte, J.; Cazenave, A.; Ramillien, G.; Le Toan, T.; Mognard-Campbell, N. Water volume change in the lower Mekong from satellite altimetry and imagery data. *Geophys. J. Int.* **2006**, *167*, 570–584.
17. Hess, L.L.; Melack, J.M.; Novo, E.M.; Barbosa, C.C.; Gastil, M. Dual-season mapping of wetland inundation and vegetation for the central Amazon Basin. *Remote Sens. Environ.* **2003**, *87*, 404–428.
18. Morrissey, L.A.; Durden, S.L.; Livingston, G.P.; Steam, J.A.; Guild, L.S. Differentiating methane source areas in arctic environments with multitemporal ERS-1 SAR data. *IEEE Trans. Geosci. Remote Sens.* **1996**, *34*, 667–673.
19. Birkett, C.M. Contribution of the TOPEX NASA radar altimeter to the global monitoring of large rivers and wetlands. *Water Resour. Res.* **1998**, *34*, 1223–1239.
20. Fung, L.; Cazenave, A. *Satellite Altimetry and Earth Science.* A Handbook of Techniques and Applications, International Geophysical Series; Academic Press: San Diego, CA, USA, 2001; Volume 69.
21. Ričko, M.; Birkett, C.M.; Carton, J.A.; Crétaux, J.F. Intercomparison and validation of continental water level products derived from satellite radar altimetry. *J. Appl. Remote Sens.* **2012**, *6*, 061710.
22. Papa, F.; Prigent, C.; Rossow, W.; Legresy, B.; Remy, F. Inundated wetland dynamics over boreal regions from remote sensing: The use of Topex-Poseidon dual-frequency radar altimeter observations. *Int. J. Remote Sens.* **2006**, *27*, 4847–4866.
23. Biancamaria, S.; Lettenmaier, D.P.; Pavelsky, T.M. The SWOT mission and its capabilities for land hydrology. *Surv. Geophys.* **2016**, *37*, 307–337.
24. Giddings, L.; Choudhury, B. Observation of hydrological features with Nimbus-7 37 GHz data, applied to South America. *Int. J. Remote Sens.* **1989**, *10*, 1673–1686.
25. Choudhury, B.J. Passive microwave remote sensing contribution to hydrological variables. In *Land Surface—Atmosphere Interactions for Climate Modeling*; Springer: Berlin, Germany, 1991; pp. 63–84.
26. Sippel, S.; Hamilton, S.; Melack, J.; Choudhury, B. Passive microwave satellite observations of seasonal variations of inundation area in the Amazon River floodplain. Brazil. *Remote Sens. Environ.* **1994**, *4*, 70–76.
27. Sippel, S.; Hamilton, S.; Melack, J.; Novo, E. Passive microwave observations of inundation area and the area/stage relation in the Amazon River floodplain. *Int. J. Remote Sens.* **1998**, *19*, 3055–3074.
28. Fily, M.; Royer, A.; Goıta, K.; Prigent, C. A simple retrieval method for land surface temperature and fraction of water surface determination from satellite microwave brightness temperatures in sub-arctic areas. *Remote Sens. Environ.* **2003**, *85*, 328–338.

29. Mialon, A.; Royer, A.; Fily, M. Wetland seasonal dynamics and interannual variability over northern high latitudes, derived from microwave satellite data. *J. Geophys. Res. Atmos.* **2005**, *110*, doi:10.1029/2004JD005697.
30. Temimi, M.; Leconte, R.; Brissette, F.; Chaouch, N. Flood monitoring over the Mackenzie River Basin using passive microwave data. *Remote Sens. Environ.* **2005**, *98*, 344–355.
31. Grippa, M.; Mognard, N.; Le Toan, T.; Biancamaria, S. Observations of changes in surface water over the western Siberia lowland. *Geophys. Res. Lett.* **2007**, *34*, doi:10.1029/2007GL030165.
32. Prigent, C.; Papa, F.; Aires, F.; Rossow, W.; Matthews, E. Global inundation dynamics inferred from multiple satellite observations, 1993–2000. *J. Geophys. Res. Atmos.* **2007**, *112*, doi:10.1029/2006JD007847.
33. Sakamoto, T.; Van Nguyen, N.; Kotera, A.; Ohno, H.; Ishitsuka, N.; Yokozawa, M. Detecting temporal changes in the extent of annual flooding within the Cambodia and the Vietnamese Mekong Delta from MODIS time-series imagery. *Remote Sens. Environ.* **2007**, *109*, 295–313.
34. Kerr, Y.; Waldteufel, P.; Wigneron, J.; Martinuzzi, J.; Font, J.; Berger, M. Soil moisture retrieval from space: The Soil Moisture and Ocean Salinity (SMOS) mission. *IEEE Trans. Geosci. Remote Sens.* **2001**, *39*, 1729–1735.
35. Parrens, M.; Wigneron, J.P.; Richaume, P.; Al Bitar, A.; Mialon, A.; Wang, S.; Fernandez-Moran, R.; Al-Yaari, A.; O'Neill, P.; Kerr, Y. Considering Combined or Separated Roughness and Vegetation Effects in Soil Moisture Retrievals. *Int. J. Appl. Earth Obs. Geoinform.* **2017**, *55*, 73–86.
36. Parrens, M.; Wigneron, J.P.; Richaume, P.; Mialon, A.; Al Bitar, A.; Fernandez-Moran, R.; Al-Yaari, A.; Kerr, Y.H. Global-scale surface roughness effects at L-band as estimated from SMOS observations. *Remote Sens. Environ.* **2016**, *181*, 122–136.
37. Schroeder, R.; McDonald, K.C.; Chapman, B.D.; Jensen, K.; Podest, E.; Tessler, Z.D.; Bohn, T.J.; Zimmermann, R. Development and Evaluation of a Multi-Year Fractional Surface Water Data Set Derived from Active/Passive Microwave Remote Sensing Data. *Remote Sens.* **2015**, *7*, 16688–16732.
38. Henderson, F.M.; Lewis, A.J. Radar detection of wetland ecosystems: A review. *Int. J. Remote Sens.* **2008**, *29*, 5809–5835.
39. Bartsch, A.; Trofaier, A.; Hayman, G.; Sabel, D.; Schlaffer, S.; Clark, D.; Blyth, E. Detection of open water dynamics with ENVISAT ASAR in support of land surface modelling at high latitudes. *Biogeosciences* **2012**, *9*, 703–714.
40. Kuenzer, C.; Guo, H.; Huth, J.; Leinenkugel, P.; Li, X.; Dech, S. Flood mapping and flood dynamics of the Mekong Delta: ENVISAT-ASAR-WSM based time series analyses. *Remote Sens.* **2013**, *5*, 687–715.
41. Santoro, M.; Wegmüller, U. Multi-temporal synthetic aperture radar metrics applied to map open water bodies. *IEEE J. Sel. Top. Appl. Earth Obs. Remote Sens.* **2014**, *7*, 3225–3238.
42. Prigent, C.; Matthews, E.; Aires, F.; Rossow, W.B. Remote sensing of global wetland dynamics with multiple satellite data sets. *Geophys. Res. Lett.* **2001**, *28*, 4631–4634.
43. Papa, F.; Prigent, C.; Aires, F.; Jimenez, C.; Rossow, W.; Matthews, E. Interannual variability of surface water extent at the global scale, 1993–2004. *J. Geophys. Res. Atmos.* **2010**, *115*, doi:10.1029/2009JD012674.
44. McCarthy, J.; Gumbricht, T.; McCarthy, T. Ecoregion classification in the Okavango Delta, Botswana from multitemporal remote sensing. *Int. J. Remote Sens.* **2005**, *26*, 4339–4357.
45. Jain, S.K.; Saraf, A.K.; Goswami, A.; Ahmad, T. Flood inundation mapping using NOAA AVHRR data. *Water Resour. Manag.* **2006**, *20*, 949–959.
46. Bergé-Nguyen, M.; Crétaux, J.F. Inundations in the inner Niger delta: monitoring and analysis using MODIS and global precipitation datasets. *Remote Sens.* **2015**, *7*, 2127–2151.
47. Xiao, X.; Boles, S.; Liu, J.; Zhuang, D.; Frolking, S.; Li, C.; Salas, W.; Moore, B. Mapping paddy rice agriculture in southern China using multi-temporal MODIS images. *Remote Sens. Environ.* **2005**, *95*, 480–492.
48. Molinier, M.; Guyot, J.L.; De Oliveira, E.; Guimarães, V. *Les Regimes Hydroiogiques de L'Amazone et de Ses Affluents*; IAHS Publication: Paris, France, 1996; pp. 209–222.
49. Frappart, F.; Papa, F.; da Silva, J.S.; Ramillien, G.; Prigent, C.; Seyler, F.; Calmant, S. Surface freshwater storage and dynamics in the Amazon Basin during the 2005 exceptional drought. *Environ. Res. Lett.* **2012**, *7*, 044010.
50. Papa, F.; Frappart, F.; Güntner, A.; Prigent, C.; Aires, F.; Getirana, A.C.; Maurer, R. Surface freshwater storage and variability in the Amazon Basin from multi-satellite observations, 1993–2007. *J. Geophys. Res. Atmos.* **2013**, *118*, doi:10.1002/2013JD020500.

51. Diegues, A.C.S. *An Inventory of Brazilian Wetlands*; Number 15; IUCN: Gland, Switzerland, 1994.
52. Frappart, F.; Seyler, F.; Martinez, J.M.; Leon, J.G.; Cazenave, A. Floodplain water storage in the Negro River basin estimated from microwave remote sensing of inundation area and water levels. *Remote Sens. Environ.* **2005**, *99*, 387–399.
53. Junk, W.J. General aspects of floodplain ecology with special reference to Amazonian floodplains. In *The Central Amazon Floodplain*; Springer: Berlin, Germany, 1997; pp. 3–20.
54. Salati, E.; Marques, J. Climatology of the Amazon region. In *The Amazon*; Springer: Berlin, Germany, 1984; pp. 85–126.
55. Marengo, J.A. Interannual variability of surface climate in the Amazon Basin. *Int. J. Climatol.* **1992**, *12*, 853–863.
56. Espinoza Villar, J.C.; Ronchail, J.; Guyot, J.L.; Cochonneau, G.; Naziano, F.; Lavado, W.; De Oliveira, E.; Pombosa, R.; Vauchel, P. Spatio-temporal rainfall variability in the Amazon Basin countries (Brazil, Peru, Bolivia, Colombia, and Ecuador). *Int. J. Climatol.* **2009**, *29*, 1574–1594.
57. Ulaby, F.T. *Microwave Remote Sensing: Active and Passive, Radar Remote Sensing and Surface Scattering and Emission Theory*; Addison-Wesley: Reading, MA, USA, 1982; Volume 2.
58. Bitar, A.; Mialon, A.; Kerr, Y.; Cabot, F.; Richaume, P.; Jacquette, E.; Quesney, A.; Mahmoodi, A.; Tarrot, S.; Parrens, M.; et al. The global SMOS Level 3 daily soil moisture and brightness temperature maps. *ESSD* **2017**, doi:10.5194/essd-2017-1.
59. Brodzik, M.J.; Billingsley, B.; Haran, T.; Raup, B.; Savoie, M.H. EASE-grid 2.0: Incremental but significant improvements for Earth-gridded data sets. *ISPRS Int. J. Geo-Inform.* **2012**, *1*, 32–45.
60. Jarvis, A.; Reuter, H.I.; Nelson, A.; Guevara, E. the CGIAR-CSI SRTM 90 m Database. Hole-Filled SRTM for the Globe Version 4. 2008. Available online: http://srtm.csi.cgiar.org (accessed on 16 May 2017).
61. Huffman, G.J.; Bolvin, D.T.; Nelkin, E.J.; Wolff, D.B.; Adler, R.F.; Gu, G.; Hong, Y.; Bowman, K.P.; Stocker, E.F. The TRMM multisatellite precipitation analysis (TMPA): Quasi-global, multiyear, combined-sensor precipitation estimates at fine scales. *J. Hydrometeorol.* **2007**, *8*, 38–55.
62. Friedl, M.A.; Sulla-Menashe, D.; Tan, B.; Schneider, A.; Ramankutty, N.; Sibley, A.; Huang, X. MODIS Collection 5 global land cover: Algorithm refinements and characterization of new datasets. *Remote Sens. Environ.* **2010**, *114*, 168–182.
63. Loveland, T.; Reed, B.; Brown, J.; Ohlen, D.; Zhu, Z.; Yang, L.; Merchant, J. Development of a global land cover characteristics database and IGBP DISCover from 1 km AVHRR data. *Int. J. Remote Sens.* **2000**, *21*, 1303–1330.
64. Bontemps, S.; Defourny, P.; Radoux, J.; Van Bogaert, E.; Lamarche, C.; Achard, F.; Mayaux, P.; Boettcher, M.; Brockmann, C.; Kirches, G.; et al. Consistent global land cover maps for climate modelling communities: current achievements of the ESA's land cover CCI. In Proceedings of the ESA Living Planet Symposium, Edimburgh, UK, 9–13 September 2013; pp. 9–13.
65. Papa, F.; Güntner, A.; Frappart, F.; Prigent, C.; Rossow, W.B. Variations of surface water extent and water storage in large river basins: A comparison of different global data sources. *Geophys. Res. Lett.* **2008**, *35*, doi:10.1029/2008GL033857.
66. Frappart, F.; Papa, F.; Famiglietti, J.S.; Prigent, C.; Rossow, W.B.; Seyler, F. Interannual variations of river water storage from a multiple satellite approach: A case study for the Rio Negro River basin. *J. Geophys. Res. Atmos.* **2008**, *113*, doi:10.1029/2007JD009438.
67. Birkett, C.M.; Beckley, B. Investigating the performance of the Jason-2/OSTM radar altimeter over lakes and reservoirs. *Mar. Geod.* **2010**, *33*, 204–238.
68. Da Silva, J.S.; Calmant, S.; Seyler, F.; Rotunno Filho, O.C.; Cochonneau, G.; Mansur, W.J. Water levels in the Amazon Basin derived from the ERS 2 and ENVISAT radar altimetry missions. *Remote Sens. Environ.* **2010**, *114*, 2160–2181.
69. Klein, L.; Swift, C. An improved model for the dielectric constant of sea water at microwave frequencies. *IEEE Trans. Antennas Propag.* **1977**, *25*, 104–111.
70. Mialon, A.; Coret, L.; Kerr, Y.H.; Sécherre, F.; Wigneron, J.P. Flagging the topographic impact on the SMOS signal. *IEEE Trans. Geosci. Remote Sens.* **2008**, *46*, 689–694.

71. Frappart, F.; Ramillien, G.; Ronchail, J. Changes in terrestrial water storage versus rainfall and discharges in the Amazon Basin. *Int. J. Climatol.* **2013**, *33*, 3029–3046.
72. Ulaby, F.; Moore, R.; Fung, A. *Microwave Remote Sensing: Active and Passive*; Advanced Systems and Applications Inc.: Dedham, MA, USA, 1986; pp. 1797–1848.